



Downscaling land surface temperature data by fusing Suomi NPP-VIIRS and landsat-8 TIR data.

Yingfang Jia^{a,b}, Yan Huang^{a,b}, Bailang Yu ^{a,b}, Qiusheng Wu ^c, Siyi Yu ^{a,b},
Junhan Wu ^{a,b} and Jianping Wu ^{a,b}

^aKey Laboratory of Geographic Information Science (Ministry of Education), East China Normal University, Shanghai, China; ^bSchool of Geographic Sciences, East China Normal University, Shanghai, China;

^cDepartment of Geography, Binghamton University, State University of New York, Binghamton, NY, USA

ABSTRACT

Land surface temperature (LST) is a key parameter of great interest in many remote sensing applications. However, no single satellite system can produce thermal infrared (TIR) images at both high spatial and temporal resolution to retrieve LST. Various algorithms have been developed to enhance the spatial or temporal resolution of TIR data in the past decades. Among them, the Spatio-temporal Adaptive Data Fusion Algorithm for Temperature mapping (SADFAT) model is one of the most widely used algorithms for fusing Landsat and Moderate Resolution Imaging Spectroradiometer (MODIS) imagery. To our knowledge, Visible Infrared Imaging Radiometer Suite (VIIRS) TIR data have not yet been used in thermal downscaling with Landsat-8 TIR data. This study aims to generate daily LST images at Landsat-8 resolution (100 m) by fusing VIIRS and Landsat-8 TIR data for the first time with the SADFAT algorithm. The results indicate that the prediction accuracy for the study area ranged from 1.1 K to 1.4 K, which suggests that VIIRS data can be used as a good alternative for MODIS data for generating daily LST images by fusing Landsat TIR data.

ARTICLE HISTORY

Received 17 March 2017
Accepted 15 July 2017

1. Introduction

A growing interest in land surface temperature (LST) has been seen in the past few decades (Zhan et al. 2013), as LST is a key parameter in analysing and modelling surface energy balance and thermal exchange (Anderson et al. 2011), hydrology (Moran, Quattrochi, and Luvall 2000), climate change (Jin, Dickinson, and Zhang. 2005), urban climate (Rozenstein et al. 2014), and urban heat island (UHI) diurnal analysis and pattern analysis (Bechtel, Zakšek, and Hoshyaripour 2012; Zakšek and Oštir 2012; Sismanidis et al. 2016). Therefore, estimating LST and investigating its spatial distribution play an important role in studying urban environmental processes and human activities. Thermal infrared (TIR) remote sensing data collected by multiple platforms have proven to be effective and reliable for monitoring the thermal environment and characteristics in urban areas (Hu et al. 2014; Quan et al. 2015; El-Shirbeny et al. 2014). The Visible Infrared Imaging Radiometer Suite (VIIRS) onboard the Suomi National Polar-Orbiting Partnership (Suomi NPP) spacecraft was launched on 28 October 2011. VIIRS has

been acquiring and delivering daily TIR images at a global-scale since November 2011. The improved capabilities of VIIRS over its predecessors can be summarized as follows (Bhatt et al. 2014; Hillger et al. 2014): 1) each granule of VIIRS data covers a larger area due to the wider swath width, 2) VIIRS images have better spatial resolution at swath edge, 3) each location is covered by up to four images (two scenes and two granules for each scene), 4) diurnal change and day-night difference of human activities can be indicated by the night-time data.

A variety of methods have been developed to derive LST images with high spatio-temporal resolution (Weng, Fu, and Gao 2014; Huang et al. 2013). The Pixel Block Intensity Modulation (PBIM) method can add spatial details to the Landsat TM thermal band (Guo and Moore 1998), but it is not suitable for urban areas (Nichol 2009). The Normalized Difference Vegetation Index (NDVI) in a finer spatial resolution can be used to predict LST of a coarser resolution (Huang et al. 2013), but NDVI does not vary significantly in the impervious surface in urban area. To solve this problem, novel methods were proposed with the artificial neural network (Yang et al. 2010) and pixel decomposition (Wang et al. 2015). The Spatial and Temporal Adaptive Reflectance Fusion Model (STARFM) was first presented to blend surface reflectance of Landsat and Moderate Resolution Imaging Spectroradiometer (MODIS) (Gao et al. 2006). Based on the STARFM method, Weng, Fu, and Gao (2014) proposed a Spatio-temporal Adaptive Data Fusion Algorithm for Temperature mapping (SADFAT) by fusing Landsat and MODIS data. Among the existing methods reported in the literature, the SADFAT algorithm is one of the most widely used methods for fusing Landsat and MODIS data.

This paper presents a method for generating high spatio-temporal resolution LST images by blending VIIRS and Landsat-8 data using the SADFAT algorithm. The contributions of the letter are as follows: 1) generating high spatio-temporal resolution LST images using the SADFAT algorithm by blending VIIRS and Landsat-8 data for the first time; 2) comparing the predicted LST with the fusion results of MODIS and Landsat-8.

2. Study area and data

2.1. Study area

Our study area focused on Beijing, China. The focused area is 51 km long in the west-east direction and 58 km wide in the south-north direction with a total area of 2958 km². It is part of the peri-urban area of Beijing Municipality and covers part of the north-eastern Beijing city and districts, including Chaoyang, Shunyi, Huairou, Miyun, Tongzhou, and Pinggu. The Beijing Capital International Airport and Huairou Reservoir are located within the area (Figure 1).

2.2. Datasets

Seven pairs of VIIRS and Landsat-8 images (Table 1) were used in this study; two pairs were used as the inputs to the SADFAT model, and the other five pairs were used as validation for the predicted results. Seven MODIS images (Table 1) with coincident acquisition dates with the Landsat images were used for results comparison. Some key satellite parameters of VIIRS, Landsat-8, and MODIS are shown in Table 2.

In this study, since the launch of the Suomi NPP on 28 October 2011, the collected images are at a nominal spatial resolution of 375 m image bands (I-bands) and 750 m in the 16 moderate-resolution bands (M-bands) as well as the DayNight Band. VIIRS can provide

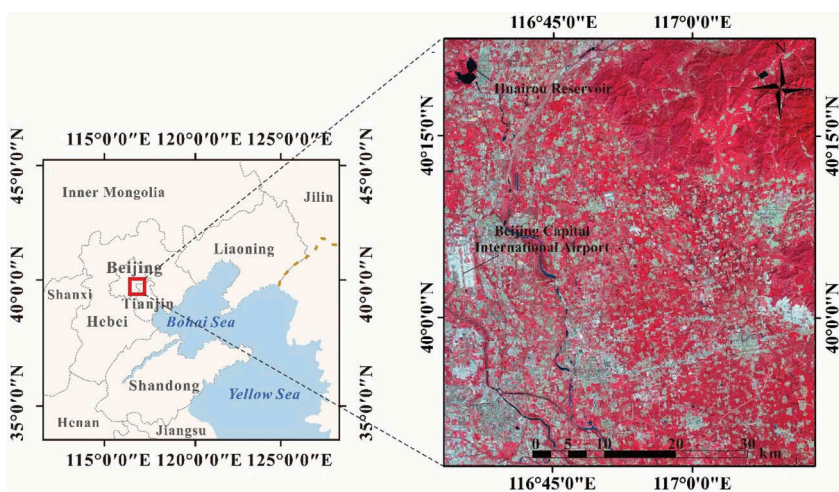


Figure 1. Location map of the study area. The image on the right is a Landsat-8 false color composite.

Table 1. Landsat-8, VIIRS, and MODIS images used in this study.

Date	Landsat-8 overpass		VIIRS overpass time	MODIS overpass time
	time			
29 April 2014	10:53		12:52	10:20
15 May 2014	10:53		12:56	10:20
19 August 2014	10:53		12:55	10:20
4 September 2014	10:54		12:59	10:20
6 October 2014	10:54		12:57	10:20
25 December 2014	10:54		12:51	10:20
16 April 2015	10:53		12:48	10:20

The overpass time recorded is the local time in the format of hour and minute.

Table 2. Satellite parameters of Landsat-8, VIIRS, and MODIS.

Parameter	Landsat 8		VIIRS	MODIS	
Satellite altitude (km)	705		830	705	
Cycle time (min)	98.9		101	98.9	
Revisit time (days)	16		1	1	
Wavelength of TIR band (μm)	10.9	12.0	11.45	11.03	12.02
Spatial resolution of TIR band (m)	30		375	1000	

remotely sensed data with reduced delivery time, improved-quality images due to the improved scan geometry, and new and improved forecasting products (Lee et al. 2006). VIIRS TIR data were obtained from the National Oceanic and Atmospheric Administration (NOAA) Comprehensive Large Array-data Stewardship System (CLASS) website (<http://www.class.ngdc.noaa.gov/>, accessed on 27 May 2017). Thermal band data were from the dataset of VIIRS Imagery Band 05 EDR (VI5BO) in VIIRS_EDR (VIIRS Imagery Environmental Data Record). Radiance in this dataset has been radiometrically corrected. LST data were from VIIRS Land Surface Temperature EDR (VLSTO) in VIIRS_EDR, which were also used to validate the predicted LST images. As Band 11 of the Landsat-8 is significantly more contaminated by stray light, only Band 10 data were used in this study. The corresponding daily MODIS images (MOD11A1, v5) covering the study area were obtained and geographically corrected by the MRTSwath tool (Jin, Dickinson, and Zhang 2005). TIR data of the seven dates (listed in Table 1) were cloud-free, which were used in this study.

The land cover data (Global Land Cover data) were produced by the National Geomatics Center of China (NGCC) with a spatial resolution of 100 m, which was used as the definition of similar pixels. While the emissivity, an input parameter in the single channel method, was obtained from the ASTER Global Emissivity Database version 3.0 (NASA JPL 2014), and the database is available from the website of NASA Land Processes Distributed Active Archive Center (LP DAAC) at http://doi.org/10.5067/Community/ASTER_GED/AG100.003 (accessed on 27 May 2017).

3. Methodology

In this study, the SADFAT model (Weng, Fu, and Gao 2014) was adopted to derive LST images at high spatio-temporal resolution by fusing VIIRS and Landsat-8 data. Figure 2 shows the workflow of the SADFAT model. Two pairs of Landsat-8 and VIIRS thermal images were used to compute the conversion coefficient and weights. The spectrally similar pixels were defined as pixels of the same land cover type. The predicted radiance image at time t_p was computed with the inputs of VIIRS image at time t_1 , conversion coefficients and combined weights using a moving window, in which the similar pixels of the central pixel were chosen in the calculation. Finally, the radiance image was converted to LST images using the single channel method (Jimenez-Munoz and Sobrino 2010).

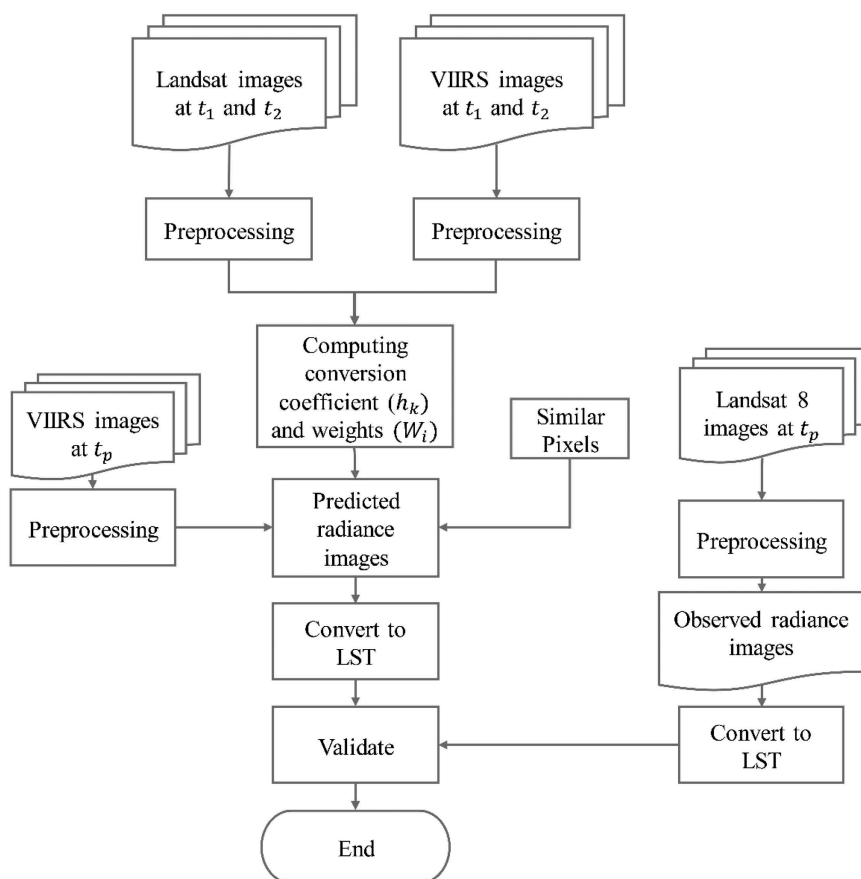


Figure 2. The procedure for generating daily LST image using Landsat-8 and VIIRS data.

With the basic theory of SADFAT model, the radiance of the thermal bands of VIIRS and Landsat-8 are related by the following equation:

$$R_L(x, y, t_p) = R_L(x, y, t_1) + \sum_{k=1}^N W_i \times h_k \times [R_V(x, y, t_p) - R_V(x, y, t_1)] \quad (1)$$

where R_L is the radiance of Landsat-8 Band 10; R_V is the radiance of VIIRS Band 15; W_i is the weight of the i th pixel in the moving window, and it consists of two parts: similarity of the i th pixel in VIIRS image and Landsat-8 image, and the distance between the similar pixel and the central pixel; h_k is the conversion coefficient for the k th land cover type, which is the ratio of the difference between the radiance of Landsat-8 Band 10 at time t_2 and time t_1 and the difference between the radiance of VIIRS Band 15 at t_2 and t_1 :

$$h_k = \frac{R_{kL}(t_2) - R_{kL}(t_1)}{R_V(t_2) - R_V(t_1)} \quad (2)$$

where $R_{kL}(t_2)$ is the radiance of k th Landsat pixel at t_2 ; $R_{kL}(t_1)$ is the radiance of the k th Landsat pixel at t_1 ; $R_V(t_2)$ is the radiance of the corresponding VIIRS pixel at t_2 ; $R_V(t_1)$ is the radiance of the corresponding VIIRS pixel at t_1 . The similarity can be calculated by the ratio of radiance of Landsat-8 and the radiance of VIIRS:

$$R_i = \begin{cases} \frac{E(L_i)}{E(V_i)} E(L_i) < E(V_i) \\ \frac{E(V_i)}{E(L_i)} E(V_i) < E(L_i) \end{cases} \quad (3)$$

where R_i is the similarity of the i th pixel; $E(L_i)$ is the radiance of i th Landsat-8 pixel; $E(V_i)$ is the radiance of i th VIIRS pixel.

The distance between the i th neighboring similar pixel and the central pixel (d_i) is the Euclidean distance; $(CW)_i$ is the combined weight, and the actual weight W_i is normalized based on the inverse:

$$(CW)_i = (1 - R_i) \times d_i \quad (4)$$

$$W_i = \left(1/(CW)_i\right) / \sum_{i=1}^N 1/(CW)_i \quad (5)$$

The predicted radiance at t_p is used to retrieve LST using the single channel method (Jiménez-Muñoz, Sobrino et al. 2014) (Equation. 6), and the atmospheric effect was corrected using the following equation. The values of Ψ_1 , Ψ_2 and Ψ_3 were computed based on the water vapour content.

$$T_s = \gamma [\varepsilon^{-1} (\Psi_1 L_{sensor} + \Psi_2) + \Psi_3] + \delta \quad (6)$$

where T_s is LST calculated by Landsat-8 TIR data; L_{sensor} is the at-satellite radiance; ε is the emissivity of the land cover type from the ASTER Global Emissivity Database 3.0; γ and δ can be calculated according to Equations (7) – (8).

$$\gamma = \left(\frac{c_2}{T_{sensor}^2} \left[\frac{\lambda^4}{c_1} L_{sensor} + \lambda^{-1} \right] \right)^{-1} \quad (7)$$

$$\delta = -\gamma L_{\text{sensor}} + T_{\text{sensor}} \quad (8)$$

where c_1 and c_2 are constants; c_1 has the value of $1.19104 \times 10^4 \text{ W}\mu\text{m}^4\text{m}^{-2} \text{ sr}^{-1}$, c_2 is $14,387.7 \text{ }\mu\text{m K}$; λ is the wavelength of the thermal infrared band of Landsat-8. T_{sensor} is the at-satellite brightness temperature, which can be calculated as:

$$T_{\text{sensor}} = \frac{K_2}{\ln\left(1 + K_1/L_{\text{sensor}}\right)} \quad (9)$$

where K_1 and K_2 are band-specific thermal conversion constants for Band 10; K_1 is $774.89 \text{ Wm}^{-2}\text{sr}^{-1}\mu\text{m}^{-1}$ and K_2 is 1321.08 K , which are given in the metadata.

The two groups of VIIRS, Landsat-8 and MODIS data on 15 May 2014 and 6 October 2014 were selected to calculate the conversion coefficient as mentioned above. To calculate the weights in the moving window, the Global Land Cover classification was used to identify similar pixel. The observed LST were directly computed from the Landsat-8 thermal infrared band using the single channel method.

4. Results and discussion

4.1. Downscaling LST results

The results of the observed LSTs and predicted LSTs are shown in [Figure 3](#). Most of the details of water, residential area, and texture of forests in the study area are presented in the predicted LST images. The results also illustrate the thermal difference of different ground objects. For example, the runways of the Beijing Capital International Airport in the west of the study area can be well distinguished. The observed LST images calculated directly by the radiance of VIIRS, Landsat-8 and MODIS, and the predicted LST images of VIIRS and MODIS were compared.

The five groups of radiance images were predicted based on the following pairs of radiance images: 29 April 2014 and 16 April 2015 were predicted from 15 May 2014, 19 August, 4 September, 25 December, 2014 were predicted from 6 October 2014. The predicted radiance images were used as inputs for the single channel method to compute LSTs. Since the VIIRS overpass time is approximately 12:50, while Landsat and MODIS are approximately 10:50 and 10:20, respectively, the conversion coefficients of VIIRS and Landsat are smaller. As a result, a cold bias can be observed in [Figure 3](#).

Scatter plots between the Landsat-observed and VIIRS- and MODIS-predicted LSTs for the five predicted dates are shown in [Figure 4](#). The closer the data points fell on the diagonal line, the better the predicted results are. As shown in [Figure 4](#), the spatial variation is overestimated since the land cover types were used to define similar pixels, but the actual surface properties have changed over time and weather. To assess the prediction accuracy, RMSE, mean difference, mean absolute difference, and correlation coefficient were computed ([Table 3](#)). Overall, the values of the correlation coefficient between the predicted and observed LSTs were quite high, ranging from 0.71 to 0.93. The correlation coefficients for the VIIRS-predicted LSTs were found to be slightly lower than those for the MODIS-predicted LSTs by 0.01–0.03, except for the one on 16 April 2015. The RMSE for VIIRS- and MODIS-predicted LSTs were 1.1–1.3 K and 0.8–1.4 K, respectively. The range of mean difference for the VIIRS-predicted LSTs was from -0.7 K to 0.8 K , which was slightly better than that of the MODIS-predicted LSTs (-1 K to 1 K) ([Table 3](#)). In the study by Weng, Fu, and Gao (2014), the mean difference was -0.5 K to 1.08 K . The mean absolute differences have the range of 1.3 K to 1.8 K for VIIRS results and 1.4 K to 2.1 K for MODIS results,

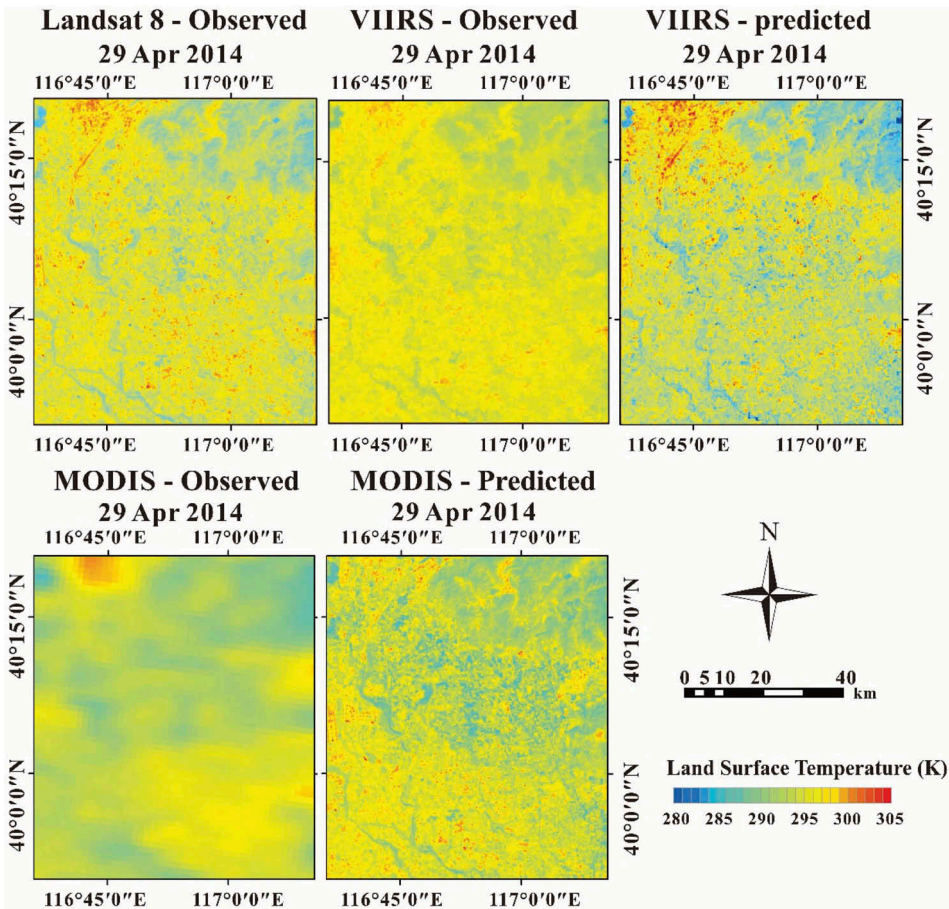


Figure 3. The observed and predicted LST images: Landsat-observed; VIIRS-observed; VIIRS-predicted; MODIS-observed; and MODIS-predicted LST images.

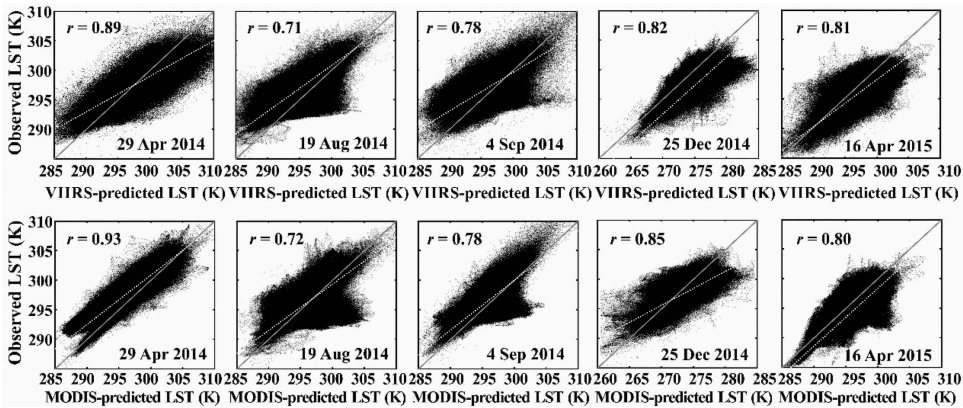


Figure 4. Scatter plots of Landsat-observed and VIIRS- and MODIS-predicted LSTs.

Table 3. The computed indices of prediction accuracy between Landsat-observed and VIIRS-predicted LSTs and between Landsat-observed and MODIS-predicted LSTs.

Date	Landsat-observed and VIIRS-predicted LSTs				Landsat-observed and MODIS-predicted LSTs			
	RMSE	Mean difference (K)	Mean absolute difference (K)	Correlation coefficient	RMSE	Mean difference (K)	Mean absolute difference (K)	Correlation coefficient
16 April 2015	1.33	0.63	1.72	0.81	1.29	−0.02	1.56	0.80
29 April 2014	1.39	0.83	1.76	0.89	1.13	−1.03	1.47	0.93
19 August 2014	1.12	−0.67	1.57	0.71	1.23	0.38	1.40	0.72
4 September 2014	1.11	−0.46	1.31	0.78	0.87	−0.83	1.39	0.78
25 December 2014	1.13	0.54	1.42	0.82	1.42	1.00	2.13	0.85

which were 1.25 K to 2.03 K in Weng, Fu, and Gao (2014). Our results indicate that using VIIRS to downscale LST can achieve similar accuracy as the results downscaled from MODIS data.

4.2. Discussions

This research predicted LST images at a high temporal frequency (daily) and at the medium spatial resolution (100 m) in the Beijing region by blending VIIRS and Landsat-8 data using the SADFAT algorithm. The VIIRS-Landsat predicted results reached an RMSE of about 1.25 K and correlation coefficient r about of 0.80. The results are similar to the MODIS-Landsat predicted results of 1.20 K and 0.81. Compared with the RMSEs of about 1.78 K and r of 0.72 using the STARFM algorithm (Gao et al. 2006), and the RMSE of about 1.69 K and R of 0.77 using the Bilateral Filtering in Beijing (Huang et al. 2013), the results of this study are better.

As VIIRS provides operational continuity with MODIS (Gao et al. 2006) with a higher spatial resolution, more spatial details are provided in VIIRS images. However, the prediction accuracy is similar to MODIS, which may be caused by the following reasons: 1) The satellite overpass time of Landsat-8 and MODIS are much closer compared to that of VIIRS (see Table 1). 2) The satellites' orbital parameters (e.g., cycle time, satellite altitude) of MODIS and Landsat are similar (Weng, Fu, and Gao 2014), of which VIIRS differs a lot. Landsat-8 and MODIS share the same satellite altitude of 705 km while the altitude of VIIRS is 803 km. The cycle time of MODIS and Landsat is 98.9 minutes, while MODIS is 101 minutes.

The prediction errors are mainly caused by the determination of similar pixels and the value of the emissivity. 1) The similar pixels are defined as the pixels that belong to the same land cover type. Since the GlobeLand30 product was produced in 2010, some land cover types may have changed. As a result, the pixels of the same land cover type may not share similar spectral signatures and characteristics anymore. It could be improved using the method of defining a threshold (Weng, Fu, and Gao 2014). 2) The emissivity data used in this study were obtained from the ASTER Global Emissivity Database 3.0, which represent the average emissivity in clear-sky days from 2000 to 2008. It provides the emissivity with a much finer resolution than assigning the emissivity for each class. However, there were some inherent limitations since the real emissivity of the ground object varies widely over time.

5. Conclusions

In this letter, we demonstrated that the combination of VIIRS and Landsat TIR data is feasible to downscale LST at a high temporal frequency and at the relatively high spatial resolution (100 m). The SADFAT model followed with the single channel algorithm was applied to

generate high spatio-temporal resolution LST images with VIIRS and Landsat-8 thermal band radiance in the Beijing district. The same model was also used for fusing Landsat-8 and MODIS data. The results were compared by statistical indicators, including the root mean square error (RMSE), mean difference, mean absolute difference, and correlation coefficient. It can be concluded that VIIRS data are also suitable to be applied to the SADFAT model, and using these two types of datasets to predict high spatial resolution LST images share similar accuracy according to the accuracy analysis. It is evident that VIIRS TIR data can be used as a good alternative for MODIS TIR data for generating daily LST images by fusing Landsat TIR data. Some limitations still exist in this study. Due to the differences in satellite overpass time and satellite parameters, some of the geometrical factors should be considered in applying the model to fuse VIIRS and Landsat-8 data in future research. We hope that this study could enlighten more applications of VIIRS TIR data.

Acknowledgments

The authors would like to thank two anonymous journal reviewers for providing insightful comments which improved the quality of the manuscript.

Disclosure statement

No potential conflict of interest was reported by the authors.

Funding

This work was supported in part by the National Natural Science Foundation of China under Grant 41471449, in part by the Natural Science Foundation of Shanghai under Grant 14ZR1412200, in part by the Innovation Program of Shanghai Municipal Education Commission (No. 15ZZ026), and in part by the Fundamental Research Funds for the Central Universities of China.

ORCID

Bailang Yu  <http://orcid.org/0000-0001-5628-0003>
 Qiusheng Wu  <http://orcid.org/0000-0001-5437-4073>
 Siyi Yu  <http://orcid.org/0000-0001-5628-0003>
 Junhan Wu  <http://orcid.org/0000-0001-5437-4073>
 Jianping Wu  <http://orcid.org/0000-0001-5437-4073>

References

- Anderson, M. C., W. P. Kustas, J. M. Norman, C. R. Hain, J. R. Mecikalski, L. Schultz, M. P. González-Dugo, C. Cammalleri, G. d'Urso, A. Pimstein, and F. Gao. 2011. "Mapping daily evapotranspiration at field to continental scales using geostationary and polar orbiting satellite imagery." *Hydrology and Earth System Sciences* 15(1): 223-239. doi: [10.5194/hess-15-223-2011](https://doi.org/10.5194/hess-15-223-2011).
- Bechtel, B., K. Zakšek, and G. Hoshyaripour. 2012. "Downscaling Land Surface Temperature in an Urban Area: A Case Study for Hamburg, Germany." *Remote Sensing* 4 (10): 3184–3200. doi:[10.3390/rs4103184](https://doi.org/10.3390/rs4103184).
- Bhatt, R., D. R. Doelling, A. S. Wu, X. X. Xiong, B. R. Scarino, C. O. Haney, and A. Gopalan. 2014. "Initial Stability Assessment of S-NPP VIIRS Reflective Solar Band Calibration Using Invariant Desert and Deep Convective Cloud Targets." *Remote Sensing* 6 (4): 2809–2826. doi:[10.3390/rs6042809](https://doi.org/10.3390/rs6042809).
- El-Shirbeny, M. A., M. A. Aboelghar, S. M. Arafat, and A. G. M. El-Gindy. 2014. "Assessment of the Mutual Impact between Climate and Vegetation Cover Using NOAA-AVHRR and Landsat Data in Egypt." *Arabian Journal of Geosciences* 7 (4): 1287–1296. doi:[10.1007/s12517-012-0791-3](https://doi.org/10.1007/s12517-012-0791-3).

- Gao, F., J. Masek, M. Schwaller, and F. Hall. 2006. "On the Blending of the Landsat and MODIS Surface Reflectance: Predicting Daily Landsat Surface Reflectance." *IEEE Transactions on Geoscience & Remote Sensing* 44 (8): 2207–2218. doi:10.1109/TGRS.2006.872081.
- Guo, L. J., and J. M. Moore. 1998. "Pixel Block Intensity Modulation: Adding Spatial Detail to TM Band 6 Thermal Imagery." *International Journal of Remote Sensing* 19 (13): 2477–2491. doi:10.1080/014311698214578.
- Hillger, D., C. Seaman, C. Liang, S. Miller, D. Lindsey, and T. Kopp. 2014. "Suomi NPP VIIRS Imagery Evaluation." *Journal of Geophysical Research* 119 (11): 6440–6455. doi:10.1002/2013jd021170.
- Hu, L. Q., N. A. Brunsell, A. J. Monaghan, M. Barlage, and O. V. Wilhelmi. 2014. "How Can We Use MODIS Land Surface Temperature to Validate Long-Term Urban Model Simulations?" *Journal of Geophysical Research-Atmospheres* 119 (6): 3185–3201. doi:10.1002/2013jd021101.
- Huang, B., J. Wang, H. H. Song, D. J. Fu, and K. Wong. 2013. "Generating High Spatio-Temporal Resolution Land Surface Temperature for Urban Heat Island Monitoring." *IEEE Geoscience and Remote Sensing Letters* 10 (5): 1011–1015. doi:10.1109/lgrs.2012.2227930.
- Jimenez-Munoz, J. C., and J. A. Sobrino. 2010. "A Single-Channel Algorithm for Land Surface Temperature Retrieval from ASTER Data." *IEEE Geoscience and Remote Sensing Letters* 7 (1): 176–179. doi:10.1109/LGRS.2009.2029534.
- Jiménez-Muñoz, J. C., J. A. Sobrino, D. Skokovic, C. Mattar, and J. Cristóbal. 2014. "Land Surface Temperature Retrieval Methods From Landsat-8 Thermal Infrared Sensor Data." *IEEE Transactions On Geoscience And Remote Sensing* 11 (10): 1840–1843. doi: 10.1109/LGRS.2014.2312032.
- Jin, M., R. E. Dickinson, and D. Zhang. 2005. "The Footprint of Urban Areas on Global Climate as Characterized by MODIS." *Journal of Climate* 18 (18): 1551–1565. doi:10.1175/JCLI3334.1.
- Lee, T. F., S. D. Miller, C. Schueler, and S. Miller. 2006. "NASA MODIS Previews NPOESS VIIRS Capabilities." *Weather Forecasting* 21 (4): 649–655. doi:10.1175/WAF935.1.
- Moran, M. S., D. A. Quattrochi, and J. C. Luvall. 2000. "Thermal Infrared Measurement as an Indicator of Plant Ecosystem Health." *Thermal Remote Sensing in Land Surface Processes*. doi:10.1201/9780203502174.
- NASA JPL. 2014. "ASTER Global Emissivity Dataset, 100-meter, HDF5." *NASA EOSDIS Land Processes DAAC*. doi:10.5067/community/aster_ged/ag100.003.
- Nichol, J. 2009. "An Emissivity Modulation Method for Spatial Enhancement of Thermal Satellite Images in Urban Heat Island Analysis." *Photogrammetric Engineering & Remote Sensing* 75 (5): 547–556. doi:10.14358/PERS.75.5.547.
- Quan, W. J., H. B. Chen, X. Z. Han, and Z. Q. Ma. 2015. "Validation of the Modified Becker's Split Window Approach for Retrieving Land Surface Temperature from AVHRR." *Journal of Meteorological Research* 29 (5): 823–836. doi:10.1007/s13351-015-4110-2.
- Rozenstein, O., Z. H. Qin, Y. Derimian, and A. Karnieli. 2014. "Derivation of Land Surface Temperature for Landsat-8 TIRS Using a Split Window Algorithm." *Sensors (Basel)* 14 (4): 5768–5780. doi:10.3390/s140405768.
- Sismanidis, P., I. Keramitsoglou, C. Kiranoudis, and B. Bechtel. 2016. "Assessing the Capability of a Downscaled Urban Land Surface Temperature Time Series to Reproduce the Spatiotemporal Features of the Original Data." *Remote Sensing* 8 (4): 274. doi:10.3390/rs8040274.
- Wang, F., Z. H. Qin, W. J. Li, C. Y. Song, A. Karnieli, and S. H. Zhao. 2015. "An Efficient Approach for Pixel Decomposition to Increase the Spatial Resolution of Land Surface Temperature Images from MODIS Thermal Infrared Band Data." *Sensors* 15 (1): 304–330. doi:10.3390/s150100304.
- Weng, Q. H., P. Fu, and F. Gao. 2014. "Generating Daily Land Surface Temperature at Landsat Resolution by Fusing Landsat and MODIS Data." *Remote Sensing of Environment* 145: 55–67. doi:10.1016/j.rse.2014.02.003.
- Yang, J., P. Gong, J. X. Zhou, H. B. Huang, and L. Wang. 2010. "Detection of the Urban Heat Island in Beijing Using HJ-1B Satellite Imagery." *China-Earth Sciences* 53: 67–73. doi:10.1007/s11430-010-4131-8.
- Zakšek, K., and K. Oštir. 2012. "Downscaling Land Surface Temperature for Urban Heat Island Diurnal Cycle Analysis." *Remote Sensing of Environment* 117 (1): 114–124. doi:10.1016/j.rse.2011.05.027.
- Zhan, W., Y. Chen, J. Zhou, J. Wang, W. Liu, J. Voogt, X. Zhu, J. Quan, and J. Li. 2013. "Disaggregation of Remotely Sensed Land Surface Temperature: Literature Survey, Taxonomy, Issues, and Caveats." *Remote Sensing of Environment* 131 (8): 119–139. doi:10.1016/j.rse.2012.12.014.